

Phenomenological theory of magnetization reversal in nanosystems with competing anisotropies

A. A. Leonov^{1,2}, U.K. Rößler¹, A.N. Bogdanov¹

¹*IFW Dresden, Postfach 270116, D-01171 Dresden, Germany and*

²*Donetsk Institute for Physics and Technology, R. Luxemburg 72, 83114 Donetsk, Ukraine*

(Dated: August 22, 2021)

The interplay between intrinsic and surface/interface-induced magnetic anisotropies strongly influences magnetization processes in nanomagnetic systems. We develop a micromagnetic theory to describe the field-driven reorientation in nanomagnets with cubic and uniaxial anisotropies. Spin configurations in competing phases and parameters of accompanying multidomain states are calculated as functions of the applied field and the magnetic anisotropies. The constructed magnetic phase diagrams allow to classify different types of the magnetization reversal and to provide detailed analysis of the switching processes in magnetic nanostructures. The calculated magnetization profiles of isolated domain walls show that the equilibrium parameters of such walls are extremely sensitive to applied magnetic field and values of the competing anisotropies and can vary in a broad range. For nanolayers with perpendicular anisotropy the geometrical parameters of stripe domains have been calculated as functions of a bias field. The results are applied to analyse the magnetization processes as observed in various nanosystems with competing anisotropies, mainly, in diluted magnetic semiconductor films (Ga,Mn)As.

PACS numbers: 75.70.-i, 75.50.Ee, 75.10.-b 75.30.Kz

I. INTRODUCTION

In magnetic nanostructures complex physical processes on surfaces and interfaces give rise to enhanced uniaxial magnetic anisotropies [1, 2, 3, 4]. The interplay between these induced and intrinsic (magnetocrystalline) anisotropies strongly influences the magnetization processes in many important classes of nanoscaled systems, such as ferromagnet-antiferromagnet bilayers [5, 6, 7, 8], thin epilayers of diluted magnetic semiconductors [9, 10, 11, 12, 13, 14] or in magnetic nanoparticles [15, 16, 17, 18, 19], and is the reason of various remarkable effects involving complex spin reorientation [10, 14, 20, 21, 22, 23, 24, 25, 26, 27, 28] and the evolution of specific multidomain states [29, 30, 31, 32, 33].

Most theoretical studies in this field are restricted to the investigations of *Stoner-Wohlfarth* processes through coherent switching [34] in models with uniaxial and cubic anisotropies [35, 36, 37, 38, 39, 40, 41]. Such theories describe magnetization reversal in a limiting case of ideally hard magnetic materials. However, in real magnetic materials the reversal processes will usually take place by the formation of heterogeneous states consisting of the competing phases and their transformation under the influence of the applied field. The analysis of such *multidomain* states in systems with competing anisotropies and their influence on magnetization reversal is the subject of this paper. These investigations can be executed within a regular micromagnetic theory [42, 43], adapted to nanoscaled systems (see e. g. Refs. 44, 45, 46).

In section II we introduce the phenomenological model and methods; in the next section we derive all possible magnetic configurations in the system, calculate their stability limits, and describe reorientation effects [42, 47, 48]. These results enable us to calculate

the parameters of the multidomain states and analyse the magnetization processes (section IV). In section V we apply our results to interpret reorientation effects and magnetization reversal as observed in experimental works on nanolayers of diluted magnetic semiconductors, FM/AFM bilayers, thin films of Heusler alloys, and magnetic nanoparticles. In section VI the calculated equilibrium parameters of the isolated domain walls and stripe domains are used to analyse recent experimental results in (Ga,Mn)As films with perpendicular anisotropy.

II. PHENOMENOLOGICAL MODEL

Within the standard phenomenological theory the magnetic energy of a nanoscale ferromagnetic sample can be written as a functional $W_m = \int w(\mathbf{r})dV$ with an energy density

$$w = A \sum_i \left(\frac{\partial \mathbf{m}}{\partial x_i} \right)^2 - \mathbf{M} \cdot \mathbf{H}^{(e)} - \frac{1}{2} \mathbf{M} \cdot \mathbf{H}^{(d)} + w_a, \quad (1)$$

where $\mathbf{m} = \mathbf{M}/M_0$ ($M_0 = |\mathbf{M}|$) is the normalized value of the magnetization vector \mathbf{M} , A is the exchange constant, and $\mathbf{H}^{(e)}$ and $\mathbf{H}^{(d)}$ are the external and demagnetizing fields, respectively. The anisotropy energy density includes uniaxial anisotropy (K_u) with the axis \mathbf{a} and cubic anisotropy (K_c) with unity vectors \mathbf{n}_j along cubic axes

$$w_a(\mathbf{M}) = -K_u (\mathbf{m} \cdot \mathbf{a})^2 - \frac{1}{2} K_c \sum_{j=1}^3 (\mathbf{m} \cdot \mathbf{n}_j)^4. \quad (2)$$

The coefficients K_u and K_c are assumed to be *positive*. Hence, \mathbf{a} and \mathbf{n}_j directions are easy uniaxial and cubic

magnetization axes, respectively.

The equilibrium distribution of the magnetization $\mathbf{M}(\mathbf{r})$ is generally spatially inhomogeneous. It can be derived directly by solving the equations minimizing the energy functional Eq. (1) together with the Maxwell equations. Thus, the micromagnetic problem is formulated as a set of non-linear integro-differential equations [43]. In many classes of magnetic systems a strongly pronounced hierarchy of magnetic interaction *scales* allows to reduce the micromagnetic problem to a set of auxiliary simplified problems [42, 43]. The procedure includes: (i) the calculation of spatially homogeneous equilibrium states by minimizing energy

$$w_0(\mathbf{M}) = -\mathbf{M} \cdot \mathbf{H} + w_a(\mathbf{M}) \quad (3)$$

in an (*internal*) magnetic field \mathbf{H} for fixed values of the material parameters in Eq. (3). The solutions of (i) are used to construct magnetic phase diagrams in components of the external magnetic field (ii) and to calculate the equilibrium parameters of multidomain patterns and the structure of domain walls (iii).

In the rest of the paper, we apply this program to the model given by Eqs. (1) and (2). In order to make transparent the representation of internal homogeneous states and the phase diagrams, we restrict our discussion to the case of co-planar arrangements of easy axes and applied fields. Generalizations of this model are discussed to the end of the next section.

III. REORIENTATION TRANSITIONS AND METASTABLE STATES

In many cases of practical interest, the direction of the uniaxial anisotropy \mathbf{a} lies in the plane spanned by two of the cubic axes \mathbf{n}_j (see Eq. (2)). To be specific we define this plane as xOz plane assuming that z is directed along \mathbf{a} . In this case energy w_0 from Eq. (3) can be written as a function of the angle θ between \mathbf{M} and \mathbf{a} . Introducing the reduced energy $\Phi(\theta) = w_0/K_c + 1/8$ one obtains

$$\Phi(\theta) = -\frac{1}{8} \cos 4(\theta - \alpha) - \varkappa \cos^2 \theta - h \cos(\theta - \psi), \quad (4)$$

where

$$\varkappa = K_u/K_c, \quad h = H/H_c, \quad H_c = K_c M_0, \quad (5)$$

α is the angle between the uniaxial \mathbf{a} and cubic \mathbf{n}_1 axis, the angle ψ defines the deviation of the magnetic field \mathbf{H} from the easy axis \mathbf{a} in the xOz -plane; correspondingly, $h_z = h \cos \psi$ is the reduced field component along the uniaxial easy direction, and $h_x = h \sin \psi$ is the perpendicular component.

Energy (4) is a function of variable θ and includes four material (control) parameters, namely, angle α , ratio \varkappa and reduced magnetic field components, h_x , h_z . Model (4) has been introduced in 1964 by Torok et al. [35] for ferromagnetic films with misorientated uniaxial and

biaxial easy magnetization directions. Previous investigations of (4) have been restricted to limiting cases of $\alpha = 0$ and $\alpha = \pi/4$ and were mostly concentrated on investigations of coherent rotation processes (Stoner-Wohlfarth regime) (see Ref. 34 and bibliography in Ref. 43). Within this approach switching processes are identified with the boundaries of the metastable states (critical astroids). In this section we give a comprehensive analysis of model (4) in the full range of the control parameters $(\alpha, \varkappa, h, \psi)$. In particular, we show that the analysis of the metastable states only is not sufficient for the understanding of magnetization reversal in nanosystems with competing anisotropies. The peculiar evolution of the potential profile (4) under the influence of the applied field and specific reorientation effects are found to be crucial for the magnetization processes in this class of magnetic materials.

The stationary solutions with the equilibrium values of θ are derived from the equation $\Phi_{\theta} = 0$:

$$h \sin(\theta - \psi) = -\frac{1}{2} \sin 4(\theta - \alpha) - \varkappa \sin 2\theta \quad (6)$$

(Here we introduce a common notation for derivatives $f(x)_{x \times k} \equiv d^k f / dx^k$). The equation for the stability lines of the solutions, $\Phi_{\theta\theta} = 0$, reads

$$h \cos(\theta - \psi) = -2 \cos 4(\theta - \alpha) - 2\varkappa \cos 2\theta \quad (7)$$

and determines the stability boundaries of the solutions together with Eq. (6). Critical points of the transitions are determined by the set of equations $\Phi_{\theta \times k} = 0$, $k = 1, 2, 3$. The degeneracy of the solutions, θ_i with $i = 1 \dots L$, that provide global energy minima in the system,

$$\Phi(\theta_1) = \Phi(\theta_2) = \dots = \Phi(\theta_L), \quad (8)$$

determines the coexistence regions between L magnetic phases and the conditions for first-order transitions in the magnetic phase diagrams. It is convenient to present the solutions $\theta(h_x, h_z, \varkappa, \alpha)$ and critical regions for (4) in a set of phase planes (h_x, h_z) parametrized by the factors α and \varkappa . We start our analysis from the limiting cases $\alpha = 0$ and $\pi/4$, and after that highlight main features of the general model (4).

For symmetric cases with the easy-axes orientations along one the cubic axis ($\alpha = 0$) and along the diagonals between them ($\alpha = \pi/4$) the Eq. (4) can be written as

$$\Phi(\theta) = \mp \frac{1}{8} \cos(4\theta) - \varkappa \cos^2 \theta - h \cos(\theta - \psi), \quad (9)$$

with “-” for $\alpha = 0$ and “+” for $\alpha = \pi/4$. Generally model (9) describes magnetic states in a planar ferromagnet with competing uniaxial (second-order) and biaxial (fourth-order) magnetic anisotropy. The model has been applied for many bulk and nanoscale magnetic systems, including reorientation effects in rare-earth orthoferrites [42, 49], several classes of intermetallic compounds [50], first-order magnetization processes in high-anisotropy materials [38], and for magnetic nanolayers with surface/interface-induced magnetic anisotropy

[3, 4, 8, 39, 40, 46, 47]. The model from Eq. (9) has also proved to be valid for diluted magnetic semiconductors as a novel class of magnetic materials [9, 10, 11, 48].

The invariance of the potential Eq. (9) under the transformation

$$\varkappa \rightarrow -\varkappa, \quad \theta \rightarrow \theta + \pi/2, \quad \psi \rightarrow \psi + \pi/2, \quad (10)$$

means that the cases with different sign of \varkappa transform into each other by rotation of the reference system through an angle $\pi/2$. This invariance allows one to restrict the analysis to positive values of \varkappa . The analysis of (9) yields four topologically different types of (h_x, h_z) -phase diagrams depending on values $\varkappa > 0$, as shown in Fig. 1.

Under transformation (10) the equations of equilibrium (6), (7) for the potential (9) with $\alpha = 0$ are converted into those equations for $\alpha = \pi/4$. Thus, for the same values of \varkappa the lability lines for both cases transform into each other by a rotation through $\pi/2$ (Fig. 1).

For $\varkappa > 5$ the lability lines have a similar shape as the *Stoner-Wohlfarth* astroid [34]. In the limit of large \varkappa , the lability line asymptotically coincides with this astroid for simple uniaxial ferromagnets. As \varkappa decreases from 5 to zero the lability lines transform into an eight-cusp line with the shape of the classical wind rose. At the parameter value $\varkappa = 5$, a bifurcation takes place by the formation of so-called “swallow tails” [46] in one pair of opposite cusps (Fig. 1(B), (F)). In the interval $5 > \varkappa > 1$, the swallow tails gradually widen, and at $\varkappa = 1$ the lower cusp points reach the horizontal axis. In the interval $1 > \varkappa > 0$ the phase diagrams have regions with overlapping swallow tails (Fig. 1(C), (G)). Finally at $\varkappa = 0$, that is for zero uniaxial anisotropy, the lability line transforms into the wind rose with eight corners. For the two special orientations of the uniaxial anisotropy in Eq. (9) with $\alpha = 0$ and $\alpha = \pi/4$ the lability lines are identical. Still, the phase diagrams are fundamentally different as they pertain to different magnetic states and different coexistence regions of metastable magnetic states. Depending on the control parameters, there are regions with $L = 2, 3$, or 4 degenerate states, and, consequently, first-order transitions involving *two*, *three* and *four* phases.

For $\varkappa > 5$ the first-order lines between *two* magnetic states are segments of straight lines connecting opposite cusp points $h_z = 0$, ($|h_x| \leq |h_x^c| = 2(\varkappa \mp 1)$) (Fig. 1(A), (E)) [46]. At zero field the transitions occur between antiparallel magnetic states $\theta_1 = 0$ and $\theta_2 = \pi$. For finite transversal magnetic fields $|h_x| < h_x^c$ the solutions for coexisting phases are determined from Eq. (6) with $h_z = 0$ and $\alpha = 0(\pi/4)$,

$$\sin^3 \theta - \frac{1 \pm \varkappa}{2} \sin \theta \pm \frac{h_x}{4} = 0. \quad (11)$$

These solutions describe a gradual decrease of the magnetization component m_z . In the endpoints of the first-order transitions $h_x = \pm h_x^c$ the magnetization vectors in both phases are perpendicular to the easy direction.

For $5 > \varkappa > 0$ the evolutions of the magnetic states within the swallow tails are different for the two models (see potential profiles in Fig. 2). For the model with $\alpha = 0$, the potential wells corresponding to the global energy minima are swapped within the swallow tails (Fig. 2(A)). Hence, different canted states become degenerate in equilibrium along lines of first-order transitions (lines a_1b_1 , a_1b_2 , a_2b_3 , a_2b_4 in Fig. 2(A)). These lines meet the transition line a_1a_2 between symmetric phases, θ_1 , $\theta_2 = \pi - \theta_1$, in the points a_1 and a_2 where *three* phases coexist. The coordinates of points a_1 and a_2 are [46, 50]

$$\tilde{h}_x = \pm 2 \sin \tilde{\theta} (\cos 2\tilde{\theta} + \varkappa), \quad \tilde{h}_z = 0 \quad (12)$$

and the solutions for the coexisting phases read

$$\theta_1 = \pm \tilde{\theta}, \quad \theta_2 = \pi \mp \tilde{\theta}, \quad \theta_3 = \pm \pi/2, \quad (13)$$

where $\sin \tilde{\theta} = (-1 + \sqrt{1 + 3\varkappa})/3$.

For the model with $\alpha = \pi/4$, the minimum in the potential is unique for the swallow tails in the parameter range $5 > \varkappa > 1$. Hence, the transformation of the energy profile involves only metastable states (Fig. 2(B)). However, the particular transformation of the metastable states in these regions plays an important role in the evolution of the domain wall profiles (see Sec. VI). In the interval $1 > \varkappa > 0$ the first order transitions arise within the region of the overlapping swallow tails. The transition line is a segment c_1c_2 , with the points $c_1 = (0; 2(\varkappa - 1))$, $c_2 = (0; -2(\varkappa - 1))$. Along this line segment *two* phases coexist with solutions θ_1 and $\theta_2 = -\theta_1$. The solutions θ_1 are given by the equation

$$\cos^3 \theta - \frac{1 + \varkappa}{2} \sin \theta - \frac{h_z}{4} = 0, \quad (14)$$

that can be derived from Eq. (6). The first-order transition line from c_1 to c_2 crosses the other transition line along $(h_x; 0)$ in the origin. Hence, in this point *four* magnetic phases coexist with

$$\theta_1 = \frac{1}{2} \arccos \varkappa, \theta_2 = -\theta_1, \theta_3 = \pi - \theta_1, \theta_4 = \pi + \theta_1. \quad (15)$$

For $\varkappa = 0$ (zero uniaxial anisotropy) both potentials (9) are converted into the model of a cubic ferromagnet. The corresponding phase diagrams (Fig. 1(D) and (H)) are identical and include two lines of first-order phase transitions between symmetric states. In the origin four degenerate phases with magnetization along the cubic easy axes \mathbf{n}_1 and \mathbf{n}_2 coexist.

In the general case with a misalignment between uniaxial and cubic easy axes given by the parameter α the potential Φ (Eq. (4)) is a periodic function of α with periodicity $\pi/2$. Thus an analysis in the range $0 \leq \alpha \leq \pi/4$ covers all physically different states. Here we describe the evolution of the (h_x, h_z) diagrams when α varies from zero to $\pi/4$. The sets of diagrams in Figs. 3 and 4 show the transformation of the transition and lability lines. The case with nonoverlapping swallow tails for the parameter range $5 > \varkappa > 1$ is presented in Fig. 3. For

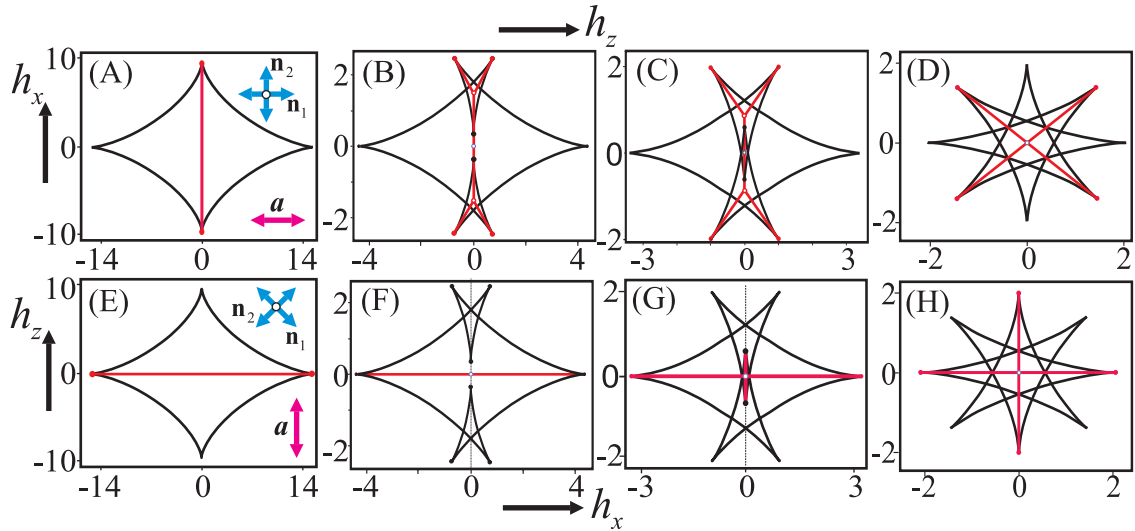


FIG. 1: (Color online) The phase diagrams of magnetic states in components of the internal magnetic field (h_x, h_z) and different values of the parameter \varkappa for the ratio of uniaxial and cubic anisotropy (Eq.5). The upper panel (A)-(D) is for systems with $\alpha = 0$, the bottom panel (E)-(H) is for systems with $\alpha = \pi/4$. Two-headed vectors show orientations of the uniaxial axis \mathbf{a} and the cubic \mathbf{n}_i axes. The plots present the topologically different types of phase diagrams: (A), (E) $\varkappa > 5$, (B), (F) $5 > \varkappa > 1$, (C), (G) $1 > \varkappa > 0$, (D), (H) $\varkappa = 0$. Black lines indicate stability limits of metastable states. Red lines give the first-order transitions between different magnetic phases (see text for details).

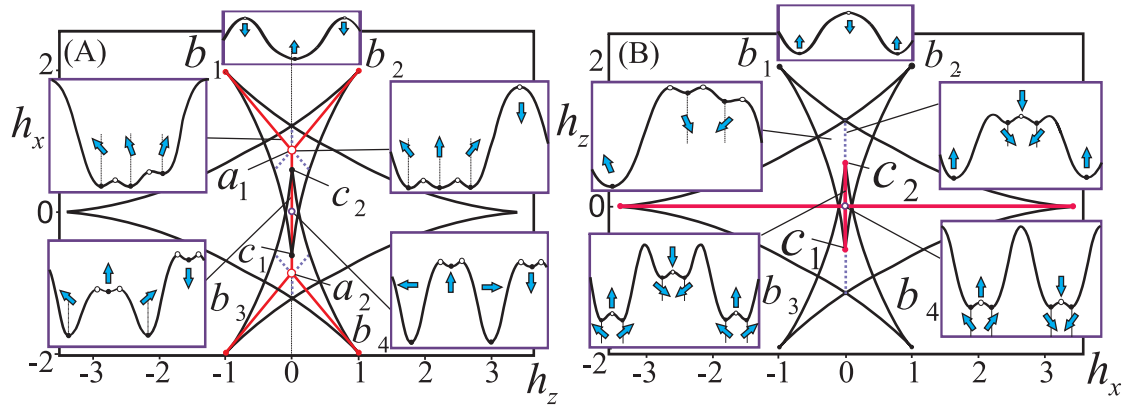


FIG. 2: The (h_x, h_z) phase diagrams for $\varkappa = 0.7$: $\alpha = 0$ (A), $\alpha = \pi/4$ (B). Potential profiles $\Phi(\theta)$ are sketched for various points in the phase diagrams to illustrate the evolution of the magnetic states in both models.

small $\alpha(\varkappa)$ two lines of the phase transitions between canted phases still exist (Fig. 3(B)). With increasing α the points a_1 and a_2 for the three-phase coexistence move to either of the cusp points b_2 and b_3 (Fig. 3(C)) After these points have merged only two-phase transition lines exist in the system (line b_1b_4 in Fig. 3(D), (E)). Thin (blue) lines in Fig. 3(B)-(F) indicate the values of the magnetic fields where two metastable states have the same energy. They are not connected with any physical processes in the system but help to understand the transformation of the energy profiles.

The phase diagram with overlapping swallow tails for the parameter range $1 > \varkappa > 0$ is shown in Fig. 4. In this case the transition lines between pairs of canted phases

in the limit $\alpha = 0$, Fig. 4(A), gradually transform into straight line segments for transitions between pairs of the symmetric phases in the limit $\alpha = \pi/4$, Fig. 4(D). During this process the points of the three-phase coexistence a_1 and a_2 move towards each other (Fig. 4(B), (C)), and merge into the point with four-phase coexistence at the origin for $\alpha = \pi/4$, Fig. 4(D).

The sets of modified astroids in Figs. 1 and 3 represent geometrical singularities studied by a special field in mathematics known as *catastrophe theory* [51]. It was found that for rather general form of potentials there exist only seven fundamental types of singularities referred to as *catastrophes* [51]. Four of them are realized in the stability lines of Figs. 1 and 3. The astroid lines, where one

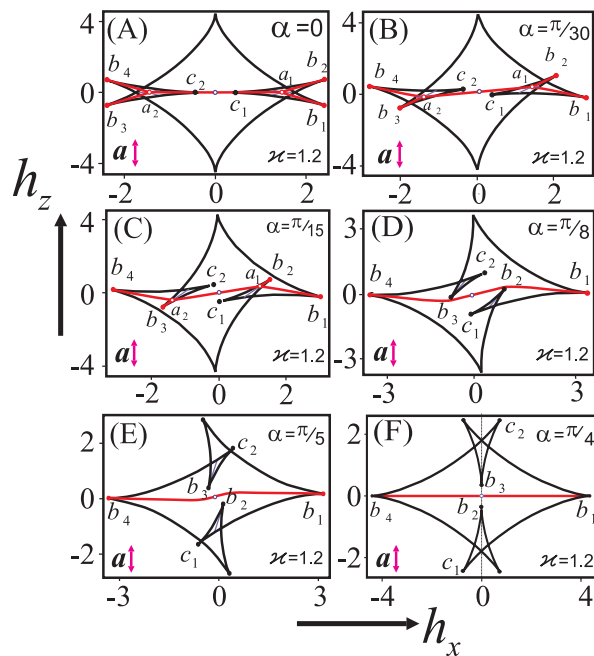


FIG. 3: (h_x, h_z) phase diagrams for $\kappa = 1.2$ and different values of α demonstrate the transformation between the two symmetric cases with $\alpha = 0$ (A) and $\alpha = \pi/4$ (F).

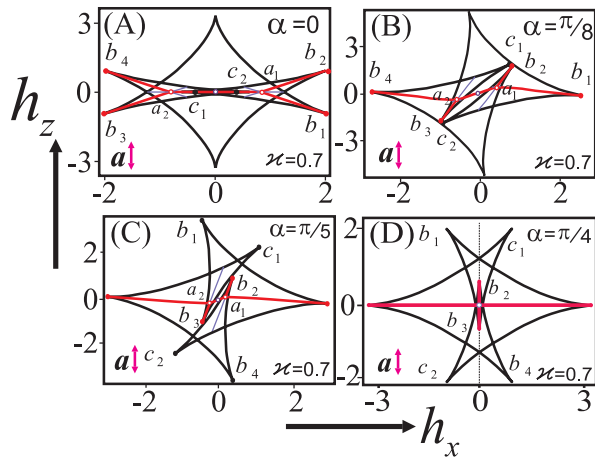


FIG. 4: (h_x, h_z) phase diagrams similar to that in the previous figure but for $\kappa = 0.7$.

local minimum merges with a local maximum, are named *fold catastrophes*. The edge points where two folds meet have two minima merging with a maximum. These singularities are known as *cusp catastrophes*. By a characteristic discord in the terminology, the feature known in magnetics as “swallow tails” as shown in Fig. 1(B), (F) are called *butterfly catastrophes* in mathematics, while the triangular regions, as those with the cusps c_1, b_2 in Fig. 3(D), are called *swallow tail catastrophes*. The lability lines in Fig. 1 belong to a family of *hypercycloids*. In present article we shall adhere to the terminology used

in micromagnetism.

The transformation of the common Stoner-Wohlfarth astroid (as 4-cusped hypercycloid- Fig. 1(A), (E)), into the 8-cusped hypercycloid with the wind rose shape (Fig. 1(D), (H)) occurs in many magnetic systems with competing anisotropies and has been investigated during the last forty years. To the best of our knowledge the 8-cusped hypercycloid has been firstly obtained in Refs. 35, 52 (see also the remarks about earlier conference contributions in Ref. 35). The transformation from the common astroids (Fig. 1) into a lability line with swallow tails, and the further evolution of these curves to the wind rose has been obtained in Ref. 35. Torok et al. also demonstrated several diagrams of lability line for model with misorientated anisotropy axes (Eq.(9)). In many following papers (see, e.g. Refs. 36, 37, 53) peculiarities of lability lines for the model (9) have been investigated. The coordinates of the critical points for (9) were calculated in Refs. 50, 54, 55, 56. The solutions for the first-order phase transition lines and the coexisting states have been carried out in Refs. 57, 58 (see also Ref. 46)). In this paper we have given an exhaustive summary of model (4).

IV. MAGNETIC PHASE DIAGRAMS

In the previous section the solutions for possible magnetic states have been presented as functions of the internal field. For ellipsoidal magnets with a homogeneous magnetization $\mathbf{M}(\mathbf{h})$ the equation [43]

$$\mathbf{h}^{(e)} = \mathbf{h} + 4\pi K_c^{-1} \hat{\mathbf{N}} \mathbf{m}(\mathbf{h}) \quad (16)$$

establishes the correspondence between magnetic phase diagrams in terms of the internal field \mathbf{h} and those in terms of the external field $\mathbf{h}^{(e)}$ ($\hat{\mathbf{N}}$ is the demagnetizing tensor). For phase diagrams in Figs. 1 and 3 the phase diagrams in external magnetic field components are plotted in Figs. 5 and 6, correspondingly.

Thin lines in Figs. 5, 6 define values of the external fields in which the internal field within the stable phases reaches the boundaries of the metastable region. The transition lines (\mathbf{h}_{tr}) in Figs. 1, 3 transform into the areas bounded by thick (red) lines in Figs. 5, 6. These areas define maximum possible regions where thermodynamically stable multidomain states of the competing phases can exist [42, 43, 59].

For $\kappa > 5$ and $\alpha = 0$ the (h_x, h_z) diagram in Fig. 1(A) converts into that in Fig. 5(A). The transition line in Fig. 1(A) transforms into an area of a two-phase multidomain state that is bounded by an ellipse (red line). For $|\kappa| < 5$ and $\alpha = 0$ the diagrams in the terms of external-field components become rather complicated: Fig. 5(B) is obtained by mapping the phase diagram in Fig. 1(B), and Fig. 5(C) by mapping Fig. 1(D). The lines of the two-phase transitions in Fig. 1(B), (C) convert into areas of two-phase domain structures (DS); the points of three-phase coexistence (12) “swell” into the triangular

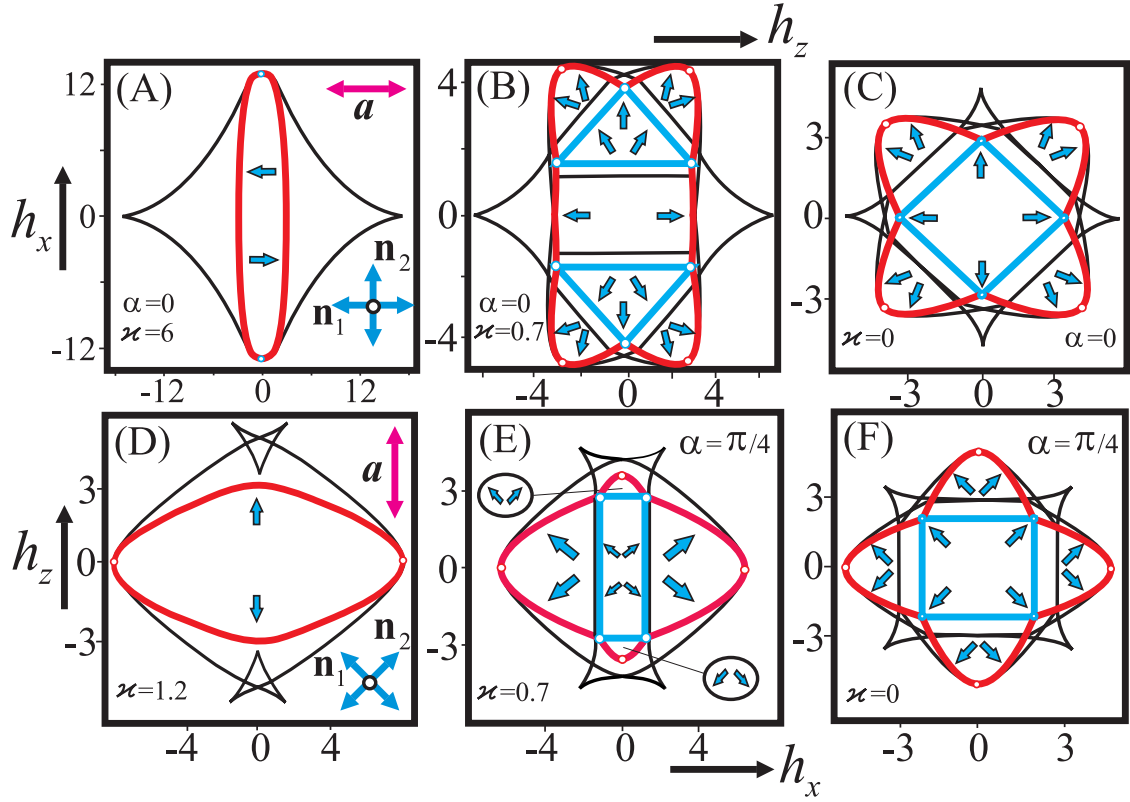


FIG. 5: Magnetic phase diagrams in the components of the external field $h_x^{(e)}$, $h_z^{(e)}$ for $\alpha = 0$ ((A)- (C)) and $\alpha = \pi/4$ ((D)- (F)). Thick lines limit regions of three- and four-phase (blue) and two-phase (red) multidomain states. Arrows show magnetic configurations in the (co-existing) domains. All calculations have been carried out for a spherical sample ($N_{ii} = 1/3$).

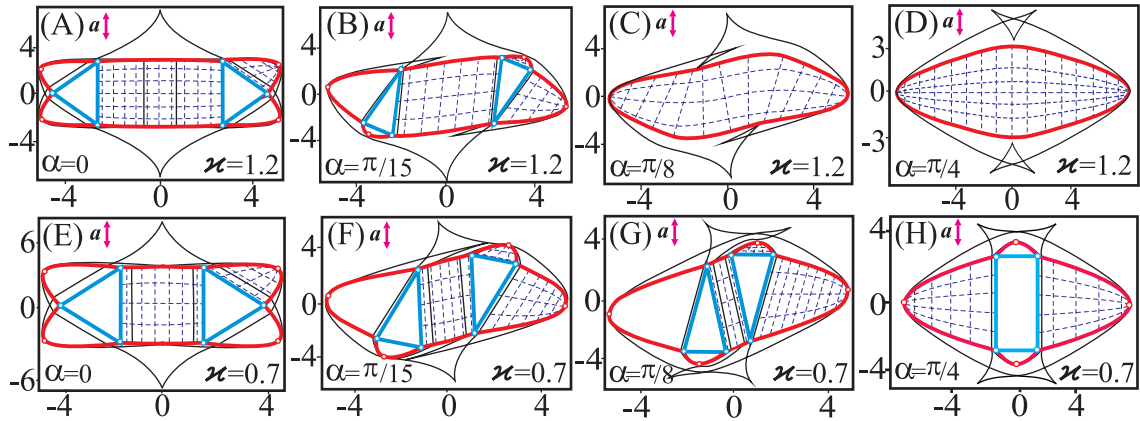


FIG. 6: Magnetic phase diagrams in the components of the external field $h_x^{(e)}$, $h_z^{(e)}$ for $\kappa = 1.2$: (A)- $\alpha = 0$; (B)- $\alpha = \pi/15$; (C)- $\alpha = \pi/8$; (D)- $\alpha = \pi/4$ and $\kappa = 0.7$: (E)- $\alpha = 0$; (F)- $\alpha = \pi/15$; (G)- $\alpha = \pi/8$; (H)- $\alpha = \pi/4$. Thin dotted lines are the lines of the constant internal field and the constant phase fractions.

regions of three-phase domain structure; and the point (0,0) in Fig. 1(D), where four phase $\theta_j = \pi j/4$ coexist, transforms into a rectangular area with a four-phase multidomain state.

The phase diagrams in Fig. 1(F), (G), (H) for systems with $\alpha = \pi/4$ are mapped into the phase diagrams in

Fig. 5(D), (E), (F), correspondingly. For $\kappa > 1$ the phase diagram in Fig. 5(D) includes one region of two-phase multidomain states and two swallowtail pockets in the metastable region. For $1 > \kappa > 0$ $\mathbf{h}^{(e)}$ -phase diagrams include a rectangular area, where four-phase domain states are stable with spin configurations in the

domains described by Eq. (15). Adjacent to this area, there are four regions in the phase diagrams with two-phase multidomain states (Fig. 5(E)). Finally the $\mathbf{h}^{(e)}$ -phase diagram for $\varkappa = 0$ in Fig. 5(F) becomes identical to that in Fig. 5(C).

For α varying from zero to $\pi/4$ the phase diagrams are plotted in the case $\varkappa = 1.2$ (Fig. 6(A)-(D)) and $\varkappa = 0.7$ (Fig. 6(E)-(H)) and reflect the complex transformation of the regions of the DS existence. For $\varkappa = 1.2$ the triangular areas of three phase DS and the regions of two phase DS deform (Fig. 6(B)) and then disappear at all (Fig. 6(C)) leading to a phase diagram with one distorted ellipse of two phase DS. The phase diagram for $\varkappa = 0.7$ demonstrate another kind of transformation. Now, the regions of three-phase DS do not disappear (Fig. 6(F), (G)) but, on the contrary, join to form a rectangular area of four phase DS (Fig. 6(H)). Here in Fig. 6, the thin dashed lines denote the lines of constant internal field and constant phase fractions (in regions of stable two-phase DS). When an external magnetic field is varied following these lines, then either domain walls are displaced or the magnetization rotates in each domain, respectively.

In the next section we apply the diagrams of solutions in Figs. 1,2,3,4 and the phase diagrams in Figs. 5,6 to analyze the magnetization processes in nanosystems with competing anisotropies. We emphasize that those diagrams describe two limiting cases of ideally hard and ideally soft magnetic behavior. In ideally hard magnetic materials magnetization processes occur via evolution of metastable states. Magnetic phases exist everywhere in their stability regions up to their boundaries (*Stoner-Wohlfarth regime*). The corresponding magnetization curves (dotted lines in Fig. 7) are characterized by the widest possible hysteresis cycles [43], and single domain states are realized in these systems. In the opposite case of ideally soft magnetic materials the magnetization reversal occurs via the evolution of *thermodynamically* stable states. Such *anhysteretic* processes involve the formation of multidomain patterns. These spatially inhomogeneous states are composed of domains formed by the competing phases of the magnetic-field induced first-order transition [42, 43]. Extended regions of multidomain states have been observed during reorientation processes in several groups of bulk magnetic systems (e. g. orthoferrites and easy-axis antiferromagnets [42, 60]). For these magnetically soft, low anisotropy systems the multidomain states are described by the phase theory equations [42, 43]. The phase theory approximation strictly is valid only if the characteristic sizes of the sample are much larger than the sizes of domains, and transitional regions between domains are localized into narrow domain walls [43]. Both these requirements are met only in ideally soft, massive magnetic samples. Thus, in soft magnetic materials the magnetization processes are mainly determined by occurrence of the first-order phase transitions and the evolution of the magnetic states in the coexistence phases during these transitions (solid lines in Fig. 7). The magnetization processes in real mate-

rials are intermediate between these two limiting cases and include both evolution of the metastable and multidomain states. In magnetic nanolayers domain sizes usually exceed the layer thickness. In magnetic nanoparticles only few domain walls are observed, and in sufficiently small particles multidomain states are completely blocked. On the other hand, coercivity of the magnetic nanosystems prevents the formation of the equilibrium states and causes hysteretic magnetization reversal.

V. COMPARISON WITH EXPERIMENT

The phase diagrams of solutions in Figs. 1-4 can be applied for explanation of magnetization processes in many nanomagnetic systems with competing anisotropies, for example, in thin films of diluted magnetic semiconductors (DMS), in ferromagnetic(FM)/antiferromagnetic(AFM) bilayers [8, 23], Heusler alloys [61], and/or nanoparticles [15, 47]. First, we consider the phase diagrams with symmetric arrangement of easy uniaxial and cubic anisotropy axes (Fig. 1,2), as applied for nanolayers of DMS. And then we give examples of systems with different values of angle α between anisotropy axes.

Layers of diluted magnetic semiconductors represent a new class of materials with a strongly pronounced competing character of the magnetic anisotropy. In existing (Ga, Mn) As nanolayers the ratio \varkappa of uniaxial and cubic anisotropy varies in a broad range and is controlled by strains, temperature and hole concentration [9, 10, 11, 12, 13, 14, 23]. The magnetization processes in $\text{Ga}_{1-x}\text{Mn}_x\text{As}$ thin films grown by molecular beam epitaxy on GaAs(001) substrates are described by the diagrams of solutions for highly symmetric geometry, $\alpha = 0; \pi/4$ (Fig. 1). The in-plane magnetization reversals in these systems are determined by the competition of cubic anisotropy with easy axes $\langle 100 \rangle$ and uniaxial anisotropy favouring the directions of $\langle 110 \rangle$ type. Thus, the solutions of (4) for $\alpha = \pi/4$ are applicable in this case (Fig. 1(E)-(H)). The main features of in-plane magnetization processes in such layers are summarized in Fig. 2(B) and were experimentally investigated in a number of works [12, 20, 21, 29].

In Ref. 29 the 300nm thick $\text{Ga}_{1-x}\text{Mn}_x\text{As}$ ($x = 0.03$) samples were studied combining direct imaging of magnetic domains and SQUID magnetometry. At temperatures above 30K the samples exhibit the uniaxial anisotropy with easy axis along [110], whereas for temperatures below 30K the magnetization vector deviates from this direction indicating the dominance of the four-fold symmetry. According to our phenomenology these magnetic films followed the temperature transition from the phase diagram in Fig. 1(F) for dominating uniaxial anisotropy ($\varkappa > 1$) to that in Fig. 1(G) with competing character of anisotropy ($\varkappa < 1$). The angle between the magnetization and the axis [110] is determined by the Eq. (15). For $T=15\text{K}$ (the ratio $\varkappa = 0.42$ was obtained from fits of the hard-axis magnetization curves and cal-

culating the easy-axis orientation from Eq.(9) this angle is 32° which agrees with experimental results. The magnetization processes for high temperature ($\varkappa > 1$, Fig. 1(F), 5(D)) proceed through the nucleation and expansion of domains with two orientations of the magnetization vector. In fields applied along the easy axis [110] the evolution of the DS is accompanied only by the 180° domain wall movement (Fig. 6(D)), and the metastable states in swallow tails (see energy profiles in Fig. 2(B)) can be considered as the nuclei of domains. During the magnetization processes along [100] axis the domains not only nucleate and expand but the magnetization rotates inside each domain of various phases (Fig. 6(D)). The magnetization reversal for low temperature ($\varkappa = 0.42$) along one of the cubic easy axes proceeds in three stages[29] through the formation of intermediate domains (Fig. 1(G), 5(E)). In the first (and the last) stage a transversely magnetized domain nucleates indicating the entering into the area of two-phase DS in Fig. 5(E). With field increasing the completely reversed domains nucleate and propagate rapidly through the sample indicating the beginning of the area with four phase DS in Fig. 5(E) [29]. It is remarkable that the one stage switching processes are also possible and are accompanied by the transformation of four phase domain structure for some directions of magnetic field (blue open points in Fig. 5(E)). The magnetization curves in Fig. 7 (A), (B) are typical for the in-plane geometry displaying biaxial character of the anisotropy. The successive switching of the magnetization in Fig. 7(A) are caused by the redistribution of the metastable minima in the energy profiles for varying magnetic field (Fig. 2(B)). The hysteresis loops of such a type are more pronounced for purely cubic anisotropy ($\varkappa = 0$) and were observed for 603 nm-Ga_{0.957}Mn_{0.043}As films [20]. If the applied magnetic field makes the angle with the [100] axis in the range $(0; \pi/4)$, and initially spins are aligned along $[\bar{1}00]$, then the first incoherent reversal is related to the appearance of domains with [010] magnetization, whereas the second jump is due to the [100] domain (Fig. 1(D)).

In Ref. 62 the character of in-plane magnetic anisotropy has been determined by means of transport measurements. All layers were patterned into 40-60 μ m wide Hall bar structures, and a strong anisotropic magnetoresistance effect provides a very convenient method to study the anisotropy at fixed temperature. The resistance polar plots of transport measurements for prevalent biaxial anisotropy [62] look similar to the phase diagram in Fig. 5(C). The [110] uniaxial anisotropy leads to the narrowing and subsequent disappearance of the four phase DS area (Fig. 5(D), (E), (F)). As well, it was shown that an additional uniaxial anisotropy with [010] easy axis is present in the system. This anisotropy results in the formation of a two phase DS region splitting the rectangle with four phases (Figs. 5(B), (C)).

The solutions with $\alpha = 0$ (Fig. 1(A)-(D)). are realized for out-of-plane magnetic field and in-plane orientation of the magnetization [21, 27, 28]. The stability lines of

phase diagrams for $\alpha = 0$ (Figs. 1(B), (F)) are similar to those for $\alpha = \pi/4$ but the magnetization processes are quite different. The triple point with three coexisting phases inside the swallow tail (Fig. 1(B)) has a crucial influence on the magnetization reversal and is the reason of specific double shifted hysteresis loops (Fig. 7(C)) observed in many works [12, 14, 27].

In Ref. 27 Ga_{1-x}Mn_xAs films grown on hybrid ZnSe/GaAs substrates with a low Mn concentration ($x \approx 0.01$) were chosen to identify the role of both types of anisotropies in the magnetic reversal process. Varying the hole concentration p and temperature T the ratios \varkappa according to Figs. 1(A)-(D) can be swept. For the hole concentration $p = 8.5 \cdot 10^{19} \text{cm}^{-3}$ the temperature progression results in the succession of phase diagrams, namely, Fig. 1(A) for T=20K, Fig. 1(B) for T=7K, Fig. 1(C) for T=3K and Fig. 1(D) for T=1.5K. The switching processes for high temperature exhibit the typical behavior of a specimen magnetized along the hard direction (Fig. 1(A)). In this case, a domain structure exists with magnetization vector tilted with respect to the magnetic field. As the temperature is lowered the triple point in Fig. 1(B) denotes the existence of an additional stable magnetization state along the magnetic field direction. Thus, the subloops of the hysteresis curves (Fig. 7(C)) reflect the jump of the magnetization into this minimum accompanied by the three phase domain structure. The variation of magnetic field in the region spanned by the swallow tails lead to various scenarios of the DS transformation (see energy profiles in Fig. 2(A)). In particular, different cases (shown in Fig. 5(B) by the red and blue open points) of the transition from multidomain states into a single domain state can be realized. For some directions of the magnetic field crossing regions with two- and three-phase DS one can observe even more complex hysteresis loops consisting of three subloops (Fig. 7(D)). In our phenomenology the maximum hysteresis loops encircle the anhysteretic magnetization curves with three and two phase DS. Experimentally that kind of magnetization processes was observed in Co₂MnSi and Co₂MnGe Heusler alloys [61]. With the temperature decreasing the subloops in Fig. 7(C) broaden around the two steps of the magnetization, and a hysteresis loop with only a weak double shift is observed (at T=1.5K, the experimentally measured value of $\varkappa \approx 0.26$ corresponds to phase diagram Fig.7(E)). Note, that one should distinguish the hysteresis loops of such type for the cases with $\alpha = \pi/4$ (Fig. 7(A)) and $\alpha = 0$ (Fig. 7(E)) because the magnetization processes are fundamentally different. For (Ga,Mn)As systems with low hole concentration ($p = 3.0 \cdot 10^{19} \text{cm}^{-3}$) uniaxial anisotropy is much larger than the cubic anisotropy [27]. This situation is described by model (4) with $\varkappa > 5$ (Fig. 1(A), 5(A)). If the magnetic field is applied along the easy axis of uniaxial anisotropy (Fig. 1(B),5(B)) then the two phase DS transforms into a single phase state. As a remnant of the DS, 360° domain walls may remain in this state and can act as nuclei of new reverse domains when lowering

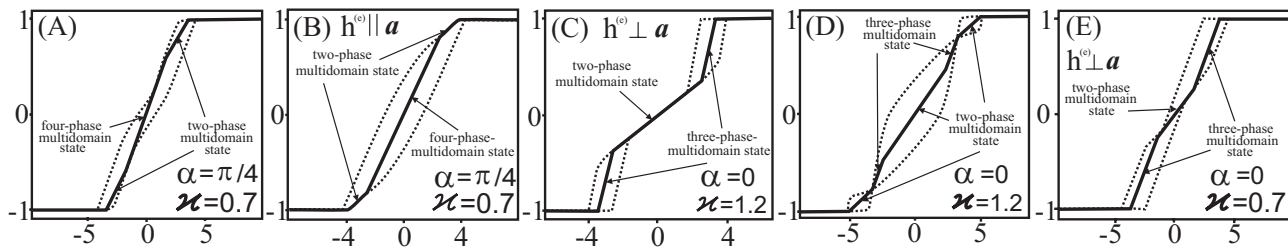


FIG. 7: Magnetization curves (schematically) for systems with two- and four-phase multidomain states (A),(B) and for those with two- and three-phase multidomain states (C)-(E).

or changing the external magnetic field. Experimentally such situations have been studied in magnetic field perpendicular to the film and for out-of-plane magnetization vector [33].

In FM/AFM bilayers of cubic materials the intrinsic cubic $\langle 100 \rangle$ anisotropy may compete with the uniaxial anisotropy induced by the exchange couplings between two layers [23]. To establish the exchange bias uniaxial anisotropy, the bilayer film is cooled in an in-plane magnetic field which determines the easy axis of induced anisotropy. In Ref. 23 the magnetization reversal has been studied in an exchange-biased $\text{CaMnO}_3/\text{La}_{0.67}\text{Sr}_{0.33}\text{MnO}_3$ bilayer film grown on vicinal $\text{SrTiO}_3 \langle 100 \rangle$ with the angle between cubic and uniaxial easy axes being $\alpha = 30^\circ$. With temperature decreasing the magnetic films followed the transition from the phase diagram of solutions in Figs. 3(E) ($T=160\text{K}$) to that in Fig. 4(C) ($T=5\text{K}$). The magnetization processes for high temperatures involve only the redistribution of a two phase DS (Fig. 6(C)). The metastable states inside each swallow tail lead only to the slight deformation of energy profiles and do not influence significantly the magnetization reversal (Fig. 3(E)). For low temperatures those metastable states become stable (Fig. 4(C)) and alternatively a domain state can be realized. The three and two phase DS (Fig. 6(F),(G)) in the system result in complex hysteresis loops with a hint of a double shift (Fig. 7(E)) [23].

Double shifted magnetization curves with strongly pronounced subloops (Fig. 7(C)) and the astroid with swallow tails (Fig. 3(A)) were observed in Ref. 8 for metallic multilayers samples with the structure $\text{Si}(100)/\text{Cu}(15\text{nm})/\text{Ni}_{80}\text{Fe}_{20}(35\text{nm})/\text{NiMn}(50\text{nm})/\text{Co}(\text{tnm})/\text{Pd}(15\text{nm})$ grown by an e-beam evaporation system. The thickness was varied between 5 nm and 25 nm. It was shown that the double-shifted hysteresis loops (and parameter \varkappa) could be tuned by several parameters, e.g., the variation of Co film thickness, and the field-annealed time.

In magnetic single-domain nanoparticles the competition of the uniaxial anisotropy due to the enhanced surface interactions and intrinsic magnetocrystalline anisotropy stabilizes different multiple magnetic states in the system with the possibility of switching between them (for details see Ref. 15). Different geometries of relative easy axes alignment are realized in these

nanoobjects. Phase diagrams with swallow tails (Fig. 6(C)) for misaligned easy anisotropy axes have been obtained for FeCuB nanoparticles [16] and Co clusters [17]. Astroids with rounded corners (Fig. 5(A)) have been observed in fcc-Co [18] and BaFeCoTiO nanoparticles [19].

In general, in many cases of practical interest the geometry with noncoplanar competing anisotropies is observed [23, 24, 25]. For example, in 50 nm thick $\text{Ga}_{0.91}\text{Mn}_{0.09}\text{As}$ thin films grown on (311)A and (311)B substrates [23] the uniaxial anisotropies with $[01\bar{1}]$ (or $[\bar{2}33]$) and $[311]$ easy axes compete with cubic anisotropy of $\langle 100 \rangle$ type. In this case three dimensional phase diagrams, parametrized by the various ratios of anisotropy coefficients and magnetic field components, have to be constructed instead of 2D diagrams of solutions. Even for considered DMS films with (001) orientation, the out-of-plane magnetization processes can be considered as coplanar only with some restrictions. Indeed, for biaxial in-plane anisotropy and magnetic field perpendicular to the film one generally has a non-coplanar arrangement of the magnetization in domains. In that case, the phase diagram in Fig. 5 (B) is only the cross-section of that more complex 3D phase diagram. But due to the degeneracy of in-plane cubic $[100]$ and $[010]$ axes with respect to the magnetic field the main peculiarities of the switching processes can be readily explained with the simple 2D phase diagram (Fig. 1(B)). Therefore, the magnetic anisotropy geometry and magnetic field orientation determine which phase diagrams of solutions (2D or 3D) is applicable in a particular case.

VI. MULTIDOMAIN PATTERNS

Multidomain patterns have been observed in a number of systems with in-plane [29] and out-of-plane magnetization [30, 31, 32, 33, 63, 64, 65, 66]. Particularly, isolated domain walls trapped in micropatterned constrictions of (Ga,Mn)As films demonstrate a number of remarkable properties [67, 68, 69, 70] and can be used in different nanoelectronic devices (e. g. as magnetoresistive elements) [67]. The fine structure of the isolated domain wall is of prime importance when different types of domain walls are observed [71]. Here in particular, we demonstrate that for the considered systems with competing anisotropies various types of domain walls exist

with large sensitivity of their appearance on material parameters and external fields. Using the results of the two previous sections we calculate the equilibrium parameters of isolated planar domain walls and derive the equilibrium parameters of stripe domains in system with out-of-plane magnetization.

A. The structure of domain walls

For a planar isolated domain wall with energy density $\Phi(\theta)$ (4) the structure is derived by optimization of the functional

$$w_{DW} = A\theta_x^2 + K_c\Delta\Phi(\theta) \quad (17)$$

with the boundary conditions $\theta_x(\pm\infty) = 0$, $\theta(+\infty) = \theta_1$, $\theta(-\infty) = \theta_2$ (x is a spatial variable across the domain wall), and $\Delta\Phi(\theta) = \Phi(\theta) - \Phi_0$, where $\Phi_0 = \Phi(\theta_1) = \Phi(\theta_2) = \{\min\Phi\}$ is the global minimum of the system. For such a one-dimensional problem (17) the Euler equation and the first integral can be written as [43]

$$2x_0^2\theta_{xx} = \Phi_\theta, \quad (18a)$$

$$x_0^2(\theta_x)^2 = \Delta\Phi(\theta) \quad (18b)$$

where $x_0 = \sqrt{A/K_c}$ is a characteristic width of the domain wall.

The domain wall profiles $\theta(x)$, their energy and characteristic sizes can be readily derived by direct integration. However, Eqs. (18a) allow to understand the main features of such solutions. The Eq. (18a) shows that the *inflection* points of the domain wall profiles $\theta(x)$ correspond to *stationary* points of potential (4) ($\Phi_\theta = 0$). The second equation (18b) shows that the larger the deviations of the energy from the minima $\Delta\Phi(\theta)$ the larger the gradients of the profiles, θ_x . Thus, the nucleation and further evolution of local minima in the metastable region causes complex reconstructions of the domain wall profiles. Transformations of the domain wall profiles have been earlier observed in easy-axis antiferromagnets and other magnetic crystals (see examples in Ref. 42). Due to the remarkable lability of the potential profiles (4) (Fig.2) this effect is expected to be strong in the systems with competing anisotropies. As an example, we derive the parameters of the domain walls for four-phase domains with the canted states (15) that are realized in the systems with $\alpha = \pi/4$, $1 > \varkappa > 0$ at zero fields.

In this case three types of domain walls can exist (Fig. 8(A)): DWI between domains with θ_1, θ_2 and θ_3, θ_4 ($\Delta\theta_I = |\theta_1 - \theta_2| = |\theta_3 - \theta_4| = \arccos \varkappa$), DW II between θ_1, θ_3 and θ_2, θ_4 ($\Delta\theta_{II} = |\theta_1 - \theta_3| = |\theta_2 - \theta_4| = \pi - \Delta\theta_I$), and DWIII of 180 type between domains θ_1, θ_4 and θ_2, θ_3 . By integration of (18b) the energy σ and the magnetization profiles for the DWI (upper signs) and DWII (lower signs) can be readily obtained as

$$\sigma = \delta_0 \left[\sqrt{1 - \varkappa^2} \mp \varkappa \arccos(\pm\varkappa) \right] \quad (19)$$

$$x = \frac{x_0}{\sqrt{2(1 - \varkappa^2)}} \ln \left(\mp \frac{\tan \theta - \tan \theta_1}{\tan \theta + \tan \theta_1} \right), \quad (20)$$

where $\delta_0 = \sqrt{AK_c}$. Depending on the ratio $1 > \varkappa > 0$ DWI with $\Delta\theta_I < 90$ becomes more favourable than DWII with $\Delta\theta_{II} > 90$ and should exhibit stronger contrast in experiment [71]. Such domain boundaries were experimentally observed in thin films of (Ga,Mn)As by Lorentz microscopy [71]. From Ref.72 and using (20) we can evaluate the DW width. For DWI at the temperature $T = 10$ (30)K we obtain $\delta = 50$ (100)nm while for DWII $\delta = 43$ (76)nm which is consistent with the experiment. Here, $A = 0.4 \cdot 10^{-12} \text{Jm}^{-1}$, $K_c = 1.18$ (0.32) Jm^{-3} , $K_u = 0.18$ (0.11) Jm^{-3} . For $\varkappa > 1$ only DWIII exist.

These domain walls are characterized by strong variation of their parameters with the applied magnetic field. At magnetic field h_z or h_x domain walls of two types are present: walls where the magnetization vector rotates less or more than 180° (Fig.8(A),(B)). Note, that for magnetic field $h_z > 2(1 - \varkappa)$ the metastable minima (Fig.2(B)) strongly influence the profile and energy of the domain. Such a remarkable modification of the structure should strongly influence magnetoresistance of domain walls (e. g. in nanoconstrictions).

In Fig.8(C),(D) domain wall profiles and typical phase portraits for the case $\alpha = 0$ ($\varkappa = 0.7$) are plotted. At applied magnetic field h_z only 360 domain walls exist. Within these walls, nuclei of the domain with π and $\pm\pi/2$ are present (see phase portrait in Fig.8(C)). In a magnetic field strong enough these nuclei disappear. So, the energy of domain wall increases, although the width decreases. By application of magnetic fields perpendicular to the easy axis \mathbf{a} in the interval $[0; a_1]$ there are walls of two types between upper and lower canted phases (Fig.8(D)). In each domain wall nuclei of domains with $\pi/2$ and $3\pi/2$, correspondingly, are present. At $h_x = h_x(a_1)$ these nuclei expand forming three-phase multidomain textures [27].

B. Parameters of stripe domains

Magnetic configurations in (Ga,Mn)As systems include a number of noncollinear two- and multi-phase states. These phases can create thermodynamically stable multidomain states [42]. For two coexisting phases with the magnetization $\mathbf{M}^{(1)}$ and $\mathbf{M}^{(2)}$ effective values of magnetization can be introduced [42]

$$M_\perp = (\mathbf{M}^{(1)} - \mathbf{M}^{(2)}) \cdot \mathbf{v}/2, \\ H = \left[\mathbf{H} - \mathbf{H}_{tr} - 4\pi(\mathbf{M}^{(1)} + \mathbf{M}^{(2)}) \right] \cdot \mathbf{v}/2. \quad (21)$$

In particular, for perpendicular magnetized (Ga,Mn)As nanolayers with $\varkappa > 5$ the phase diagrams of magnetic states (Fig. 1,(A),(E)) are similar to those for uniaxial ferromagnets. In this case $M_\perp = M_0$ and domains are separated by 180° domain walls [43]. According to Eq.(21) the problem of multidomain states for two-phase noncollinear states can be reduced to a ferromagnetic

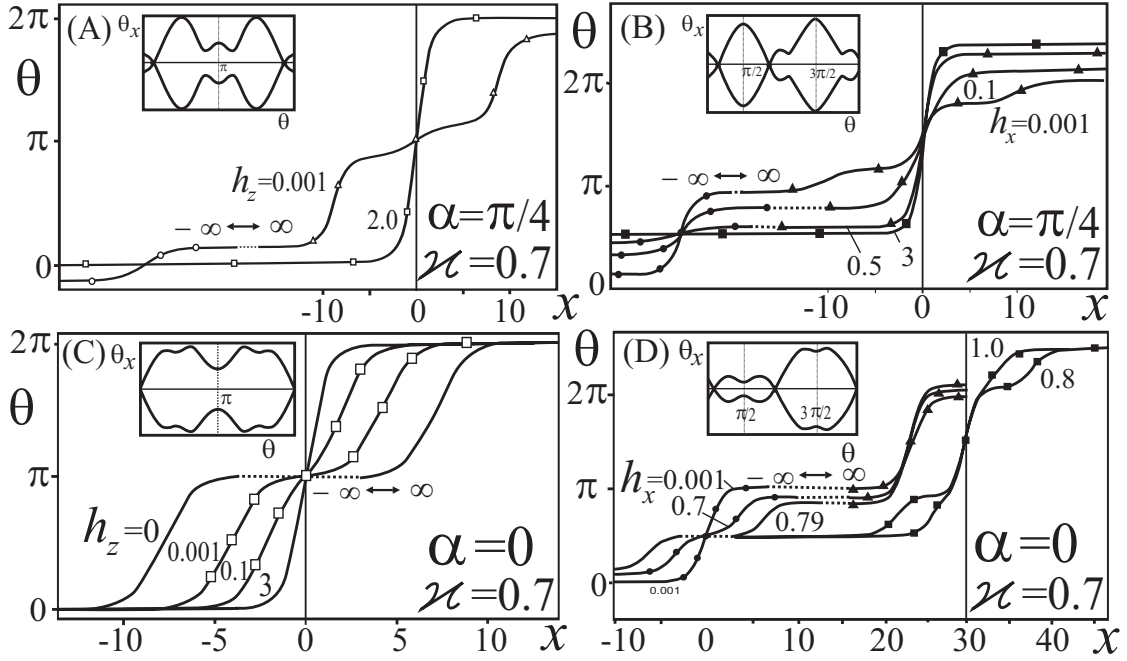


FIG. 8: Domain wall profiles for $\kappa = 0.7$: (A), (B)- $\alpha = \pi/4$, (C), (D) - $\alpha = 0$. Corresponding energy profiles are plotted in Fig. 2. Insets show the phase plane $(\theta; \theta_x)$ where $\theta_x = d\theta/dx$ (See Eq.(18)).

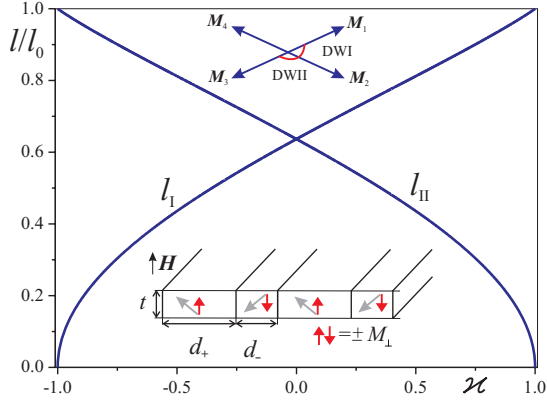


FIG. 9: Characteristic lengths $l_{I(II)}$ for stripe domains with DWI (DWII) in four-phase state ($l_0 = \pi\sqrt{AK_c}/(4M_0^2)$).

collinear domain structure with up and down magnetization M_\perp in a bias field H (\mathbf{v} is the unity vector perpendicular to the layer plane, \mathbf{H}_{tr} is the transition field between the phases $\mathbf{M}^{(1)}$ and $\mathbf{M}^{(2)}$) [42]. Similar multidomain texture are formed in the systems with a number of coexisting phases larger than two. For example, for $-1 < \kappa < 1$, $\alpha = 0$ the magnetic configurations (Eq. (15)) create four-phase multidomain states. In a layer with $\mathbf{a} \parallel \mathbf{v}$ these textures can be described by a model of ferromagnetic domains with the magnetization $M_\perp = M\sqrt{(1+\kappa)}/2$. (Fig. 9).

With effective values of the magnetization M_\perp and bias field H (21) the energy density of a (Ga,Mn)As nanolayer with stripe domains can be reduced to the well-studied model of ferromagnetic stripes [43, 73, 74]

$$w = 2\pi M_\perp^2 \left[w_m + \frac{2\Lambda p}{\pi^2} - \frac{Hq}{2\pi M_\perp} \right] \quad (22)$$

with the stray field energy density given by

$$w_m = 1 - \frac{2p}{\pi^2} \int_0^1 (1-\tau) \ln \left[1 + \frac{\cos^2(\pi q/2)}{\sinh^2(p\tau/2)} \right] d\tau, \quad (23)$$

where $p = 2\pi t/D$, $q = (d_+ - d_-)/D$, t is the layer of thickness t , $D = d_+ + d_-$ is the stripe period, and d_\pm are domain sizes with up and down magnetization (Fig. 9). The dimensionless parameter $\Lambda = \sigma(\kappa)/(4M_\perp(\kappa)^2 t) = \pi l(\kappa)/t$ measures the ratio between the domain wall energy σ and the stray field energies. It scales with the characteristic length $l(\kappa) = \sigma/(4\pi M_\perp^2)$ as the relevant material parameter [43]. Minimization of (22) with respect to p and q derives the solutions for the geometric parameters d_\pm as functions of three control parameters of model (23): the layer thickness t , the bias field H , and factor Λ . These solution have been investigated in detail (see [43, 73, 74] and bibliography in Ref. [43]). Particularly, it was shown that the solutions for stripes exist only below certain critical field $H < H^*(\Lambda) < 4\pi M_\perp$ [74]. As the bias field approaches H^* the stripes gradually transform into the homogeneous state by unlimited growth of the period ($D \rightarrow \infty$). However, at the critical field the domain of the minority phase preserves a finite

size $d_-(H^*) = d_-^*$. At higher fields ($H^* > H > 4\pi M_\perp$) it exists as a metastable state gradually shrinking to zero size at the saturation field.

In perpendicular magnetized (Ga,Mn)As layers the period of multidomain patterns exceed their thicknesses [30, 33, 66]. For such large stripes ($D \geq t$) the expansion of the integral (23) allows to simplify the problem [73]. After some algebra, the solutions for stripes can be derived in analytical form as a set of parametrical equations

$$\begin{aligned} D(H) &= \pi ut / \sqrt{1 - (H/H^*)^2}, \\ d_\pm &= (D/\pi) \arccos(\mp H/H^*), \end{aligned} \quad (24)$$

$$H^*(u) = 4\pi M_\perp f(u), \quad 2\Lambda = g(u). \quad (25)$$

Here we introduce parameter $u = d_-^*/t$ and functions

$$\begin{aligned} f(u) &= [2 \arctan 1/u - u \ln(1 + 1/u^2)] / \pi, \\ g(u) &= (1 + u^2) \ln(1 + u^2) - u^2 \ln(u^2). \end{aligned} \quad (26)$$

According to (24) at zero field $D(0) = D_0 = \pi tu$, thus, the ratio $D_0/d_-^* = \pi$. It means that at the transition field the domain of the minority phase becomes approximately six times narrower than the domain size at zero field ($D_0/2$). Within this approximation the equilibrium magnetization in the stripe phase equals

$$\langle M \rangle = M_\perp q = (2M_\perp/\pi) \arccos(H/H^*). \quad (27)$$

Finally, in the limit of large domains $D \gg t$, $D_0 = \pi t \exp(\Lambda - 1/2)$, and the transition fields for stripe and bubble domains becomes exponentially small, e. g. transition field $H^* = 4M_\perp \exp(-\Lambda + 1/2)$, the bubble collapse field $H_c = 16M_\perp \exp(-\Lambda - 1/2)$, and ratio $H^*/H_c = e/4 = 0.6796$ [73].

These results show that the solutions of magnetic domains in (Ga,Mn)As layers should demonstrate general features similar to those in uniaxial ferromagnets. However, there is an important difference between these two systems. In uniaxial ferromagnets the characteristic length is expressed as a combination of basic magnetic parameters (constants of uniaxial anisotropy K , exchange stiffness A and saturation magnetization M): $l_f = \sigma_f / (4\pi M^2) = \sqrt{AK} / (\pi M^2)$ depends only on values of uniaxial anisotropy K . On the contrary, in the diluted magnetic semiconductors the characteristic length $l(\varkappa)$ strongly depends on the values of competing magnetic anisotropies and varies in a broad range providing a complex behaviour of multidomain patterns in these materials. Eqs. (24), (25), (27) connect equilibrium parameters of stripe domains with material parameters of (Ga,Mn)As systems (4). For this model calculations of M_\perp and the domain wall energy σ allow to express Λ as a function of κ and α . For example, for four-phase domains (Eq. (15)) the magnetization and the domain

wall energies (Eq. (19)) yield functions $l_{I(II)}(\varkappa)$ plotted in Fig. 9.

Stripe domains have been observed in a number of (Ga,Mn)As nanolayers [30, 31, 32, 33, 63, 64, 65, 66]. In Table I we collect experimental data (indicated by bold) and the calculated stripe domains parameters (by solving Eqs. (24), (25), (27)) for (Ga,Mn)As layers (a-c), an yttrium-iron garnet film (d) and FePd nanolayers (e,f). For thin layers of (Ga_{0.957}Mn_{0.043})As for $T = 9$ K (1) and $T = 80$ K (2) [30] we use the experimental values of t and D_0 to calculate other parameters of stripes. For a layer (Ga_{0.93}Mn_{0.07})As at $T = 80$ K [66] we use t and a value of the transition field $H^*/(4\pi M_\perp)$ to calculate l , Λ and domain sizes D_0 and d_-^* . For comparison we derive stripe domain parameters for an epitaxial garnet film Y_{1.88}Lu_{0.2}Ca_{0.92}Ge_{0.92}Fe_{4.08}O₁₂ [75], and for FePd nanolayers [76]. According to [66] the saturation magnetization in (Ga_{0.93}Mn_{0.07})As $M_s = 28$ kA/m. Then, from the calculated value of the characteristic length we derive $\sigma = 49.0 \mu\text{J}/\text{m}^2$ (for comparison, in the (Y,Fe) garnet film $M_s = 13.6$ kA/m, and $\sigma = 110 \mu\text{J}/\text{m}^2$ [75]).

In garnet films and other classical materials with perpendicular anisotropy regular stripe domains are observed, if the layer thickness is considerably larger than the characteristic length. In such systems the equilibrium domain sizes at zero field D_0 do not exceed the layer thicknesses ($D_0 \leq t$). When films becomes thinner than l (e.g. in the vicinity of the compensation temperature of ferrimagnets [73]) the demagnetization forces are too weak to overcome coercivity and the formation equilibrium domains is impeded. As a result such multidomain patterns consist of very large domains with irregular boundaries [43]. Similar disordered domains and strongly hysteretic behaviour have been observed in (Ga,Mn)As films with perpendicular anisotropy [30, 32, 64, 65, 66]. It means that the equilibrium multidomain state are hardly reached in these systems. For example, in (Ga_{0.93}Mn_{0.07})As layers the observed width of the minority stripe at the critical field is $d_-^* = 1.7 \pm 0.3 \mu\text{m}$ [66], and about one order larger than the calculated equilibrium value ($d_-^* = 0.2 \mu\text{m}$). Up to now only few results on experimental investigations of multidomain states in perpendicularly magnetized (Ga,Mn)As nanolayers have been reported. New detailed investigations involving modern experimental methods developed in other fields of nanomagnetism (see e.g. [77]) are desirable. The results of this section

establish important physical connections with multidomain states in other classes of perpendicular magnetized materials and provide a theoretical basis for future research.

VII. SUMMARY AND CONCLUSIONS

We have developed some micromagnetic methods [42, 43] which give a consistent description of magnetization processes and multidomain structure in systems with

TABLE I: Parameters of the stripe domains in (Ga,Mn)As layers (a-c), a (Y,Fe) garnet film (d) and FePd nanolayers (e,f). They include experimental values (bold) and the results derived from model (22). Here, t is the layer thickness, l is the characteristic length, $\Lambda = \pi l/t$ is the dimensionless parameter measuring the ratio between the domain wall energy and the stray field energy (see Eqs. (22),(23)), D_0 is the equilibrium period at zero field, d_-^* is the equilibrium size of the minority phase at $H = H^*$, the transition field into the homogeneous state, Eq. (25).

	$t, \mu\text{m}$	$l, \mu\text{m}$	Λ	$D_0, \mu\text{m}$	$d_-^*, \mu\text{m}$	$H^*/(4\pi M_\perp)$
(a). (Ga _{0.957} Mn _{0.043})As [30]	0.2	0.132	2.07	3.0	0.95	$6.6 \cdot 10^{-2}$
(b). (Ga _{0.957} Mn _{0.043})As [30]	0.2	0.220	3.45	12.0	3.82	$1.7 \cdot 10^{-2}$
(c). (Ga _{0.93} Mn _{0.07})As [66]	$5 \cdot 10^{-2}$	0.10	1.920	0.643	0.2038	$3.9 \cdot 10^{-2}$
(d). (Y,Fe) garnet film [75]	11.0	0.47	0.1342	12.50	3.0	0.6
(e). FePd nanolayer [76]	$3.6 \cdot 10^{-2}$	$9 \cdot 10^{-3}$	0.7526	0.13	$3.9 \cdot 10^{-2}$	0.2612
(f). FePd nanolayer [76]	$1.15 \cdot 10^{-2}$	$9 \cdot 10^{-3}$	2.477	0.26	$8.3 \cdot 10^{-2}$	$4.4 \cdot 10^{-2}$

competing anisotropies such as diluted magnetic semiconductors.

Theoretically constructed phase diagrams in external field components in the limiting case of ideally soft magnetics allow to understand the creation of equilibrium domain structure [29], within hysteretic magnetization reversal, and explain various parts of magnetization curves (Fig.7). Thus, magnetic phase diagrams allow to put in good order and classify a vast amount of experimental data on reorientation effects, multidomain processes, and magnetization reversal in (Ga, Mn) As systems. These diagrams also give opportunity to predict change of magnetic states of the system in zero magnetic field under action of temperature [30, 31, 32] and in the case of arbitrary angle α between competing anisotropy axes [24, 25].

It is also shown that the applied magnetic field causes drastic transformations of the domain wall profile and strongly influences its parameters. Domain walls can serve as nuclei of domains for a new phase. At certain

values of the magnetic field a domain wall can be divided into domains of a new phase and two types of new domain walls. At certain critical endpoints of phase coexistence, domain walls can disappear by the rotation of the magnetization in adjacent domains towards each other.

For nanolayers with perpendicular anisotropy the geometrical parameters of stripe domains have been calculated as functions of a bias field.

Acknowledgments

The authors thank J. McCord, V. Neu, and R. Schäfer for helpful discussions. Work supported by DFG through SPP1239, project A8. A.A.L. and A.N.B. thank H. Eschrig for support and hospitality at IFW Dresden.

-
- [1] J.I. Martin, J. Nogues, K. Liu, J.L. Vicente, I.K. Schuller, J. Magn. Magn. Mater. **256**, 449 (2003).
 - [2] S.D. Bader, Surface Science **500**, 172 (2002).
 - [3] M.T. Johnson, P.J.H. Bloemen, F.J.A. den Broeder, J.J. de Vries, Rep. Prog. Phys. **59**, 1409 (1996).
 - [4] F.J.A. den Broeder, W. Hoving, and P.J.H. Bloemen, J. Magn. Magn. Mater. **93**, 562 (1991).
 - [5] R. Chang, J.S. Yang, J.C.A. Huang, C.H. Lai, J. Phys. Chem. Sol. **62**, 1737 (2001).
 - [6] Y.J. Tang, X. Zhou, X. Chen, B.Q. Liang, W.S. Zhan, J. Appl. Phys **88**, 2054 (2000).
 - [7] Z.H. Wang, G. Cristiani, H.U. Habermeier, A.C. Bland, Phys. Rev. B **72**, 054407 (2005).
 - [8] C.H. Lai, Y.H. Wang, C.R. Chang, J.S. Yang, Y.D. Yao, Phys. Rev. B **64**, 094420 (2001).
 - [9] A.H. Macdonald, P. Schiffer, N. Samarth, Nature Materials **4**, 195 (2005).
 - [10] M. Sawicki, Acta Physica Polonica A, **106**,119 (2004).
 - [11] T. Dietl, J. König, A.H. MacDonald, Phys. Rev. B **64**, 241201 (2001).
 - [12] M. Sawicki, Matsukura, A. Idziaszek, T. Dietl, G.M. Schot, C. Reuster, C. Gould, G. Karczewski, G. Schmidt, W. Molenkamp, Phys. Rev. B **70**, 245325 (2004).
 - [13] M. Sawicki, K.-Y. Wang, K.W. Edmonds, R.P. Campion, C.R. Staddon, N.R.S. Farley, C.T. Foxon, E. Papis, E. Kamińska, A. Piotrowska, T. Dietl, B.L. Gallagher, Phys. Rev. B **71**, 121302(R) (2005).
 - [14] M. Sawicki, J. Magn. Magn. Mater **300**, 1 (2006) .
 - [15] A.A. Leonov, I.G. Dragunov, A.N. Bogdanov, Appl. Phys. Lett. **90**, 193112 (2007).
 - [16] N. Duxin, M. P. Pileni, W. Wernsdorfer, B. Barbara, A. Benoit, D. Mailly, Langmuir **16**, 11 (2000).
 - [17] M. Jamet, W. Wernsdorfer, C. Thirion, V. Dupuis, P. Melinon, A. Perez, and D. Mailly, Phys. Rev. B **69**, 024401 (2004).
 - [18] W. Wernsdorfer, C. Thirion, N. Demoncy, H. Pascard, and D. Mailly, J. Magn. Magn. Mater. **242-245**, 132 (2002).
 - [19] W. Wernsdorfer, E. Bonet Orozco, K. Hasselbach, A. Benoit, D. Mailly, O. Kubo, H. Nakano, and B. Barbara, Phys. Rev. Lett. **79**, 4014 (1997).
 - [20] G.P. Moore, J. Ferre, A. Mougou, M. Moreno, L. Däweritz, J. Appl. Phys. **94**, 4530 (2003).
 - [21] X. Liu, Y. Sasaki, J. K. Furdyna, Phys. Rev. B. **67**, 205204 (2003).
 - [22] U. Welp, V.K. Vlasko-Vlasov, A. Menzel, H. D. You, X.

- Liu, J.K. Furdyna, T. Wojtowicz, Appl. Phys. Lett. **85**, 260 (2004).
- [23] K. Y. Wang, M. Sawicki, K.W. Edmonds, R.P. Champion, S. Maat, C.T. Foxon, B.L. Gallagher, T. Dietl, Phys. Rev. Lett. **95**, 217204 (2005).
- [24] A. Pross, S.J. Bending, K.Y. Wang, K.W. Edmonds, R.P. Champion, C.T. Foxon, B.L. Gallagher, M. Sawicki, J. Appl. Phys. **99**, 093908 (2006).
- [25] K.Y. Wang, K.W. Edmonds, L.X. Zhao, M. Sawicki, R.P. Champion, B.L. Gallagher, C.T. Foxon, Phys. Rev. B **72**, 115207 (2005).
- [26] M. Albrecht, G. Hu, I. L. Guhr, T. C. Ulbrich, J. Boneberg, P. Leiderer, G. Schatz, Nature Materials **4**, 203 (2005).
- [27] L.V. Titova, M. Kutrovski, X. Liu, R. Chakarvorty, W.L. Lim, T. Wojtowicz, J.K. Furdyna, M. Dobrowolska, Phys. Rev. B **72**, 165205 (2005).
- [28] X. Liu, W.L. Lim, L.V. Titova, M. Dobrowolska, J.K. Furdyna, M. Kutrowski, T. Wojtowicz, J. Appl. Phys. **98**, 063904 (2005).
- [29] U. Welp, V.K. Vlasko-Vlasov, X. Liu, J.K. Furdyna, T. Wojtowicz, Phys. Rev. Lett. **90**, 167206 (2003).
- [30] T. Shono, T. Hasegawa, T. Fukumura, F. Matsukura, H. Ohno, Appl. Phys. Lett. **77**, 1363 (2000).
- [31] T. Fukumura, T. Shono, K. Inaba, H. Koinuma, F. Matsukura, T. Hasegawa, H. Ohno, Physica E **10**, 135 (2001).
- [32] A. Pross, S. Bending, K. Edmonds, R.P. Champion, C.T. Foxon, B. Gallagher, J. Appl. Phys. **95**, 7399 (2004).
- [33] L. Thevenard, L. Largeau, O. Mauguin, G. Patriarche, A. Lemaître, N. Vernier, J. Ferré, Phys. Rev. B. **73**, 195331 (2006).
- [34] E.C. Stoner, E.P. Wohlfarth, Philos. Trans. R. Soc. London **A420**, 559 (1948).
- [35] E.J. Torok, H.N. Oredson, A.L. Olson, J. Appl. Phys. **35**, 3469 (1964).
- [36] A. I. Mitsek, Phys. Status Solidi B **59**, 309 (1973).
- [37] A. I. Mitsek, N. P. Kolmakova, and D. I. Sirota, Fiz. Met. Metalloved. **38** (1), 35 (1974).
- [38] G. Asti, F. Bolzoni, Theory of 1st order magnetization processes. J. Magn. Magn. Mater. **20**, 29 (1980).
- [39] Y. T. Millev, J. R. Cullen, H. P. Oepen, J. App. Phys. **83**, 6500 (1998).
- [40] H. P. Oepen, Y. T. Millev, H. F. Ding, S. Putter, J. Kirschner, Phys. Rev. B **61**, 9506 (2000).
- [41] A. Thiaville, J. Magn. Magn. Mater. **182**, 5 (1998).
- [42] V. G. Baryakhtar, A. N. Bogdanov, D. A. Yablonskii, Usp. Fiz. Nauk **156** (1), 47 (1988) [Sov. Phys.Usp. **31**, 810 (1988)].
- [43] A. Hubert, R. Schäfer, *Magnetic Domains*, Springer, Berlin 1998.
- [44] A. N. Bogdanov, U. K. Röbner, Phys. Rev. Lett. **87**, 037203 (2001).
- [45] A. N. Bogdanov, U. K. Röbner, K.-H. Müller, J. Magn. Magn. Mater. **238**, 155 (2002).
- [46] I.E. Dragunov, S.V. Bukhtiyarova, I.V. Zhikharev, A.N. Bogdanov, U.K. Röbner, Fiz. Tverd. Tela **48**, 1504 (2006), [Phys. Solid State **48**, 1591 (2006)].
- [47] U.K. Röbner, S.V. Bukhtiyarova, I.V. Zhikharev, A.N. Bogdanov, J. Magn. Magn. Mater. **290-291**, 772(2005).
- [48] A. N. Bogdanov, I.E. Dragunov, U. K. Röbner, J. Magn. Magn. Mater. **316**, 225 (2007).
- [49] K. I. Belov, A. K. Zvezdin, A. M. Kadomtseva, R. Z. Levitin, Usp. Fiz. Nauk **119**, 447 (1976) [Sov. Phys.Usp. **19**, 574 (1976)].
- [50] D. Melville, W. Khan, and S. Rinaldi, IEEE Trans.Magn. **12** (6), 1012 (1976).
- [51] T. Poston and I. Stewart, Catastrophe Theory and Its Applications, Pitman, London, 1978.
- [52] A. Yelon, O. Voegeli, E. W. Pugh, J. Appl. Phys. **36**, 101 (1965).
- [53] E.J. Torok, J. Appl. Phys. **36**, 952 (1965).
- [54] C. R. Chang, D. R. Fredkin, J. Appl. Phys. **63**, 3435 (1988).
- [55] C. R. Chang, D. R. Fredkin, J. Appl. Phys. **69**, 2431 (1991).
- [56] M. I. Kaganov, A. A. Yagubov, Fiz. Met. Metalloved. **36** (6), 1127 (1973).
- [57] A. N. Bogdanov, I. Ya. Granovskii, Fiz. Tverd. Tela (Leningrad) **29** (10), 2913 (1987) [Sov. Phys. Solid State **29** (10), 1674 (1987)].
- [58] V. G. Baryakhtar, A. N. Bogdanov, D. A. Yablonskii, Fiz. Tverd. Tela (Leningrad) **29** (10), 116 (1987) [Sov. Phys. Solid State **29** (10), 65 (1987)].
- [59] A. N. Bogdanov, I. E. Dragunov, Fiz. Nizk. Temp. **24**, 1136 (1998) [Low. Temp. Phys. **24**, 852 (1998)].
- [60] A. N. Bogdanov, A. V. Zhuravlev, U. K. Röbner, Phys. Rev. B **75**, 094425 (2007).
- [61] F.Y. Yang, C.H. Chang, C.L. Chien, T. Ambrose, J.J. Krebs, G.A. Prinz, V.I. Nikitenko, V.S. Gornakov, A.J. Shapiro, R.D.Shull, Phys. Rev. B **65**, 174410 (2002).
- [62] K. Pappert, C. Gould, M. Sawicki, J. Wenish, K. Brunner, G. Schmidt, L.W. Molenkamp, New Journal of Phys. **9**, 354 (2007).
- [63] D.Y. Shin, S.J. Chung, S. Lee, X. Liu, J.K. Furdyna, Phys. Rev. Lett. **98**, 047201 (2007).
- [64] L. Thevenard, L. Largeau, O. Mauguin, A. Lemaître, K. Khazen, H.J. von Bardeleben, Phys. Rev. B **75**, 195218 (2007).
- [65] A. Dourlat, V. Jeudy, C. Testelin, F. Bernardot, K. Khazen, C. Gourdon, L. Thevenard, L. Largeau, O. Mauguin, A. Lemaître, J. Appl. Phys. **102**, 023913 (2007).
- [66] C. Gourdon, A. Dourlat, V. Jeudy, K. Khazen, L. Thevenard, A. Lemaître, Phys. Rev. B **76**, 241301 (2007).
- [67] J.J. Versluijs, M.A. Bari, J.M.D. Coey, Phys. Rev. Lett **87**, 026601 (2001).
- [68] M. Yamanouchi, D. Chiba, F. Matxukura, H. Ohno, Nature (London) **428**, 539 (2004).
- [69] J. Honolka, S.Masmanidis, H.X. Tang, M.L. Roukes, D.D. Awschalom, J. Appl. Phys. **97**, 063903 (2005).
- [70] A. W. Holleitner, H. Knotz, R.C. Myers, A.C. Gossard, D.D. Awschalom, J. Appl. Phys. **97**, 10D314 (2005).
- [71] A. Sugawara, T. Akashi, P.D. Brown, R.P. Champion, T. Yoshida, B.L. Gallagher, A. Tonomura, Phys. Rev. B **75**, 241306(R) (2007).
- [72] A. Sugawara, H. Kasai, A. Tonomura, P.D. Brown, R.P. Champion, K.W. Edmonds, B.L. Gallagher, J. Zemen, T. Jungwirth Phys. Rev. Lett. **100**, 047202 (2008).
- [73] A. N. Bogdanov, D. A. Yablonskii, Fiz. Tverd. Tela **22**, 680 (1980), [Sov. Phys. Solid State **22**, 399 (1980)].
- [74] C. Kooy, U. Enz, Philips Res. Repts. **15**, 7 (1960).
- [75] A. H. Boeck, E. Della Torre, *Magnetic Bubbles*, North-Holland Publishing Company, Amsterdam 1975.
- [76] V. Gehanno, Y. Samson, A. Marty, B. Gilles, A. Chamberod, J. Magn. Magn. Mater. **172**, 26 (1997).
- [77] O. Hellwig, A. Berger, J. B. Kortright, E. E. Fullerton, J. Magn. Magn. Mater. **319**, 13 (2007).